Non-equilibrium scaling laws in axisymmetric turbulent wakes

T. Dairay[1], M. Obligado[1] and J.C. Vassilicos[1] †

[1] Turbulence, Mixing and Flow Control Group, Department of Aeronautics, Imperial College London, London SW7 2AZ, United Kingdom

(Received ?; revised ?; accepted ?. - To be entered by editorial office)

We present a combined Direct Numerical Simulation and Hot Wire Anemometry study of an axisymmetric turbulent wake. The data lead to a revised theory of axisymmetric turbulent wakes which relies on the mean streamwise momentum and turbulent kinetic energy equations, self-similarity of the mean flow, turbulent kinetic energy, Reynolds shear stress and turbulent dissipation profiles, non-equilibrium dissipation scalings and an assumption of constant anisotropy. This theory is supported by the present data up to a distance of 100 times the wake generator's size which is as far as these data extend.

Key words: Wakes, turbulence theory, turbulence simulation

1. Introduction

Over the last 60 years, the axisymmetric turbulent wake has been extensively studied experimentally and numerically (see for example Brown & Roshko 2012; Johansson *et al.* 2003, for a historical review). A basic problem of particular interest is the scaling with streamwise distance x of the wake width δ and the centreline velocity deficit u_0 (Tennekes & Lumley 1972; Bevilaqua & Lykoudis 1978; Townsend 1976; George 1989). As stated in Johansson *et al.* (2003), this problem "has puzzled researchers for more than a half-century since measured results have been either inconclusive or contradictive". The equilibrium similarity analysis of George (1989) has shown that two scalings are possible for the streamwise evolutions of the wake width and the velocity deficit. The classical equilibrium high Reynolds number scaling is obtained by assuming, as in Townsend (1976) and George (1989), that the turbulence dissipation rate ε scales as $\varepsilon = C_\varepsilon K^{3/2}/\delta$ where $C_\varepsilon = const$ and K is the turbulent kinetic energy. This leads to the high Reynolds number scalings

$$\frac{u_0(x)}{U_\infty} \sim \left(\frac{x - x_0}{\theta}\right)^{-2/3} \tag{1.1}$$

$$\frac{\delta(x)}{\theta} \sim \left(\frac{x - x_0}{\theta}\right)^{1/3} \tag{1.2}$$

where U_∞ is the freestream velocity, θ is the momentum thickness and x_0 is a virtual origin which comes out naturally from the analysis. George (1989) (see also Johansson *et al.* 2003) has shown that another, different, scaling is present when the viscous term in the mean momentum equation is not negligible. This is a low Reynolds number regime

† Email address for correspondence: j.c.vassilicos@imperial.ac.uk

for which $\varepsilon \sim \nu K/\delta^2$, where ν is the kinematic viscosity of the fluid. These low Reynolds number scalings are

$$\frac{u_0(x)}{U_\infty} \sim Re_G \left(\frac{x-x_0}{\theta}\right)^{-1} (\theta/L_b) \tag{1.3}$$

$$\frac{\delta(x)}{\theta} \sim Re_G^{-1/2} \left(\frac{x-x_0}{\theta}\right)^{1/2} (L_b/\theta)^{1/2} \tag{1.4}$$

where Re_G is a global Reynolds number determined by the inlet conditions and L_b is a reference length scale characterising the wake generator. The low Reynolds number regime has only been observed at very large distances from the wake generator by Johansson *et al.* (2003) who found it in the temporally evolving wake simulation data of Gourlay *et al.* (2001). However, no transition to this regime has been observed in the recent work of Redford *et al.* (2012) where the classical high Reynolds number scalings were recovered for very long times in their temporally evolving simulations (equivalent to very long streamwise distances). Note, however, that one of the simulations of Redford *et al.* (2012) did return the scalings $u_0(x)/U_\infty \sim x^{-1}$ and $\delta(x)/\theta \sim x^{1/2}$, but at higher local Reynolds numbers and earlier times than those where the classical predictions (1.1) and (1.2) appear.

Recently, Nedić *et al.* (2013*b*,*a*) used non-axisymmetric plates with irregular edges (see figure 1) and showed that the turbulent wakes they generate when placed normal to a freestream is at least as axisymmetric as turbulent wakes generated by axisymmetric disks. These multiscale wake generators combine wake-like with jet-like behaviours and their turbulent wakes obey wake laws which are different from the usual axisymmetric turbulent wake laws. Nedić *et al.* (2013*b*) have argued that these new scaling laws for the wake width and centreline velocity deficit can be explained in terms of the similarity analysis for axisymmetric wakes of George (1989) and are as follows:

$$\frac{u_0(x)}{U_\infty} \sim \left(\frac{x-x_0}{\theta}\right)^{-[2/(3-n)]} Re_G^{2(n-m)/(3-n)} (L_b/\theta)^{-[2n/(3-n)]} \tag{1.5}$$

$$\frac{\delta(x)}{\theta} \sim \left(\frac{x-x_0}{\theta}\right)^{[1/(3-n)]} Re_G^{(m-n)/(3-n)} (L_b/\theta)^{-[n/(3-n)]} \tag{1.6}$$

where the presence of the exponents m and n is caused by the assumption made on the turbulence dissipation scaling. Indeed, these new wake laws are direct consequences of the assumed non-equilibrium dissipation law (see Vassilicos 2015)

$$\varepsilon = C_\varepsilon \frac{K^{3/2}}{\delta} \quad \text{with } C_\varepsilon \sim Re_G^m/Re_l^n \tag{1.7}$$

where Re_l is a local Reynolds number based on local velocity and length scales. As reported in Vassilicos (2015), the values of m and n in the non-equilibrium high Reynolds number region of grid-generated turbulence are $m \approx 1 \approx n$.

Adopting $n = m = 1$ for axisymmetric turbulent wakes, the scaling laws (1.5) and (1.6) become

$$\frac{u_0(x)}{U_\infty} \sim \left(\frac{x-x_0}{\theta}\right)^{-1} (\theta/L_b) \tag{1.8}$$

$$\frac{\delta(x)}{\theta} \sim \left(\frac{x-x_0}{\theta}\right)^{1/2} (L_b/\theta)^{1/2} \tag{1.9}$$

The hot wire anemometry measurements performed by Nedić *et al.* (2013*b*) have shown

that the streamwise distance power laws in (1.8) and (1.9) hold over a very substantial streamwise region of turbulent wakes generated by their multiscale plates. In a recent numerical study, de Stadler *et al.* (2014) also reported the non-equilibrium scaling laws (1.8) and (1.9) in the wake generated by a sphere. However, because neither Nedić *et al.* (2013*b*) nor de Stadler *et al.* (2014) provided information on the turbulence dissipation, the presence of the new dissipation law (1.7) in their turbulent axisymmetric wakes could not be directly confirmed.

The main purpose of this paper is to use Direct Numerical Simulation (DNS) and Hot Wire Anemometry (HWA) measurements of axisymmetric turbulent wakes of a fractal/multiscale-edge plate placed normal to the incoming flow to carefully establish each one of the assumptions leading to the predictions such as (1.5) and (1.6) and in particular the existence of the new non-equilibrium dissipation law (1.7). The very significant advantage of fractal/multiscale-edge plates for wind tunnel experiments of turbulent wakes is that they produce much higher local Reynolds numbers than regular-edge plates with the same surface area. This way the plate's surface can be chosen small enough for the streamwise extent over which the wake is measured to be as long as possible without the velocity deficit dropping to values so low that HWA measurements become too challenging. A low surface area plate also imposes a low blockage in the wind tunnel which is also an advantage.

We start with a detailed DNS assessment of the boundary layer approximation of the mean momentum equation. The axisymmetry and self-similarity/self-preservation properties of the flow are then examined both experimentally and computationally. Finally, the streamwise evolution and scalings of the turbulence dissipation rate are studied both with DNS and HWA leading to a study of the consistency between the velocity deficit and wake width scalings and the non-equilibrium dissipation law.

The flow configuration is described in section 2. The numerical methods are described in section 3 and the experimental setup in section 4. The leading and the negligible terms in the Reynolds-averaged momentum balance are established in section 5 and the axisymmetry of the flow is established in section 6. The self-similarity properties of mean profiles are analysed in section 7 and the new dissipation law (1.7) is discussed in section 8. In section 9 we develop a revised approach to the prediction of the wake width and velocity deficit which we compare with our numerical and experimental data. Finally, the main results are summarised in section 10.

2. Flow configuration

In the present study, turbulent wakes are generated by a bluff plate of surface area A with irregular edge periphery (allowing the formation of jet-wake flows) placed normal to the laminar free stream (see figure 1 right). This irregular plate is the same as one of those used in Nedić *et al.* (2013*b*). The perimeter shape of this plate results from a geometric self-similar process leading, if continued *ad infinitum*, to a plate with fractal perimeter of infinite length and fractal dimension $D_f = 1.5$ but the same surface area A. A schematic view of the generic flow configuration considered in both the experiments and the DNS is presented in figure 1 (left). In the Cartesian coordinate system $(O; x, y, z)$, the domain is $\Omega = [-x_p, L_x - x_p] \times [-L_y/2, L_y/2] \times [-L_z/2, L_z/2]$ where x_p is the longitudinal location of the plate and the origin O is located at the center of the plate. The reference length L_b of the flow is defined by $L_b = \sqrt{A}$. For the sake of simplicity the radial distance $r = \sqrt{y^2 + z^2}$ and the polar angle $\varphi = \arctan(y/z)$ are also introduced hereinafter. The lateral dimensions of the domain L_y and L_z are the same for the wind tunnel experiments and the DNS with $L_y = L_z = 15L_b$. However, the streamwise dimension considered for

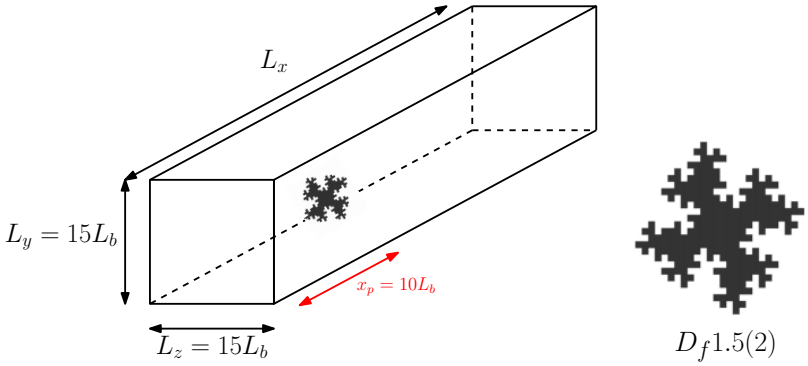

FIGURE 1. Schematic view of the flow configuration (left) and drawing of the irregular plate used to generate a turbulent wake (right).

the DNS is twice the length of the wind tunnel's test section with $L_x^{DNS} = 2L_x^{HWA} = 120L_b$. Because the plate is located at $x_p = 10L_b$ in both cases, the measurements are taken up to $x = 50L_b$ for the experiments and $x = 110L_b$ for the DNS. In the DNS case, results are reported in the range $x \in [5L_b; 100L_b]$ to avoid spurious effects due to the outflow boundary conditions. The boundaries of the domain are: (i) the flow inlet at $x = -x_p = -10L_b$; (ii) the lateral boundaries at $y = \pm L_y/2$ and $z = \pm L_z/2$; (iii) the outlet at $x = L_x - x_p$.

In the DNS case, mean quantities $\langle f \rangle_{\varphi,t}(x,r)$ of a field $f(x,r,\varphi,t)$ are estimated by averaging over time and over the homogeneous polar direction φ in the cylindrical coordinate system (x,r,φ). In the case of the HWA measurements, the mean quantity $\langle f \rangle_t(x,r)$ is estimated by averaging over time only. For simplicity, both notations are replaced by $\langle f \rangle(x,r)$ in this paper, the context making the detailed meaning of the notation clear. The mean streamwise velocity component $\langle u_x \rangle(x,r)$ is denoted U. A schematic view of the axisymmetric wake is presented in figure 2 with some definitions. The momentum thickness is defined by

$$\theta^2 = \frac{1}{U_\infty^2}\int_0^\infty U_\infty\left(U_\infty - U\right) r dr = const. \tag{2.1}$$

and the wake's width is here characterised by the integral wake's width

$$\delta^2(x) = \frac{1}{u_0}\int_0^\infty \left(U_\infty - U\right) r dr \tag{2.2}$$

where $u_0(x) = U_\infty - U(x, r/L_b = 0)$ is the centreline velocity deficit. To be unambiguous, these definitions rely on axisymmetry in the HWA case. To avoid negative values of the velocity deficit $U_\infty - U$ due to the finite size of the domain, a local freestream velocity $U_\infty = U(x,R)$ is used in these definitions where $R = 5L_b$ is the maximum radial location considered for the DNS. For the experiments, U_∞ is taken to be the maximum value of the mean velocity profile at each streamwise location, i.e. $U_\infty = \max_r(U)$.

The global Reynolds number Re_G of the flow is based on the reference length $L_b = \sqrt{A}$ and the freestream velocity U_∞;

$$Re_G = \frac{U_\infty L_b}{\nu} \tag{2.3}$$

where ν is the (constant) kinematic viscosity. The local Reynolds number Re_l is defined

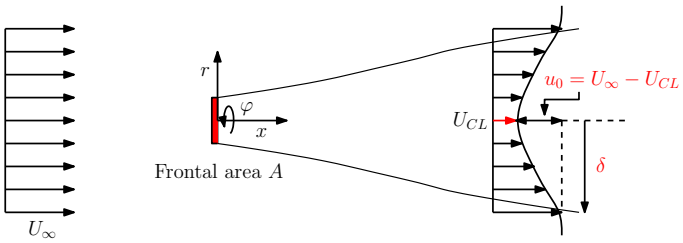

FIGURE 2. Axisymmetric wake coordinates and definitions.

Cases	Working length	Re_G
HWA	$50L_b$	40000
DNS	$110L_b$	5000

TABLE 1. Summary of the two different cases considered in this study.

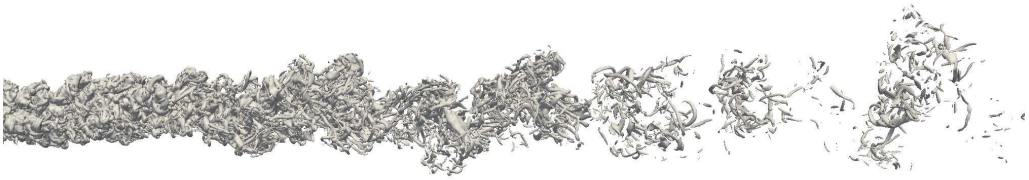

FIGURE 3. Instantaneous visualisation of an isosurface of vorticity magnitude $||\omega|| = 2$ for the *DNS* simulation. The streamwise range plotted here is from $x = 5L_b$ to $x = 45L_b$ corresponding approximately to the experimental work section.

by

$$Re_l = \frac{\sqrt{K_0}\delta}{\nu} \tag{2.4}$$

where K_0 is the turbulent kinetic energy at a centreline location.

Two cases, summarized in table 1, are considered in the present study. The HWA case refers to experiments carried out at $Re_G = 40000$ and the DNS case to a numerical simulation performed in a similar flow configuration but at $Re_G = 5000$ because of the highly demanding computations of the present DNS.

To conclude this section and for illustrative purposes only, an instantaneous visualisation of the turbulent wake generated by the DNS is plotted in figure 3 for a streamwise range corresponding approximately to the length of the experimental test section.

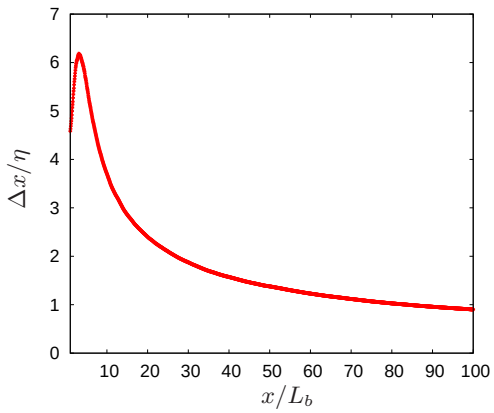

FIGURE 4. Streamwise evolution of the ratio $\Delta x/\eta$.

3. Numerical methods

The finite difference code "Incompact3d" (Laizet & Lamballais 2009; Laizet *et al.* 2010) is used to solve the incompressible Navier-Stokes equations

$$\frac{\partial \mathbf{u}}{\partial t} + \frac{1}{2}\left(\nabla \cdot (\mathbf{u} \otimes \mathbf{u}) + (\mathbf{u} \cdot \nabla)\,\mathbf{u}\right) = -\frac{1}{\rho}\nabla p + \nu \Delta \mathbf{u} + \mathbf{f} \tag{3.1}$$

$$\nabla \cdot \mathbf{u} = 0 \tag{3.2}$$

where $\mathbf{u} = (u_x, u_y, u_z)^T$ is the velocity, p the pressure and ρ (constant) the density of the fluid. The convective terms are written in the skew-symmetric form to enable reduction in aliasing errors and improvement of kinetic energy conservation for the spatial discretization used in the code (Kravchenko & Moin 1997). The modelling of the plate is performed by an Immersed Boundary Method, following a procedure proposed by Parnaudeau *et al.* (2008). The present method is a direct forcing approach that ensures the zero-velocity boundary condition at the plate walls. It mimics the effects of a solid surface on the fluid via the additional forcing term $\mathbf{f}$ in the Navier-Stokes equations. Inflow/outflow boundary conditions are assumed in the streamwise direction with a uniform fluid velocity U_∞ without turbulence as inflow condition and a 1D convection equation as outflow condition. The boundary conditions in the two spanwise directions are periodic. The computational domain $L_x \times L_y \times L_z = 120L_b \times 15L_b \times 15L_b$ is discretized on a Cartesian grid of $n_x \times n_y \times n_z = 3841 \times 480 \times 480$ points. In terms of Kolmogorov microscale η, as illustrated in figure 4, the spatial resolution is at worst $\Delta x = \Delta y = \Delta z \approx 6\eta$ (where the turbulence is at its most intense) and at best $\Delta x = \Delta y = \Delta z \approx 0.8\eta$ (at the end of the computational domain where the turbulence has decayed). In the range $10 \leqslant x/L_b \leqslant 100$, which is the range of interest of our study, the spatial resolution is always below 4η. In a recent resolution study, Laizet *et al.* (2015) have shown that a spatial resolution of 7η or 5η is sufficient to reproduce experimental results on one-point first and second order statitistics with an error margin of about 10% or 5% respectively. They also showed that quantities such as the turbulence dissipation rate require a resolution of at least 4η to be well captured. For the spatial derivatives, sixth-order centred compact schemes (Lele 1992) are used. To control the residual aliasing errors, a small amount of numerical dissipation is introduced only at scales very close to the grid cutoff. This very targeted regularization is ensured by the differentiation of the viscous term that is sixth-order accurate (Lamballais *et al.* 2011). The time integration is performed using an explicit third-order Adams-Bashforth scheme with a time step $\Delta t = 5 \times 10^{-3} L_b/U_\infty$. Full details

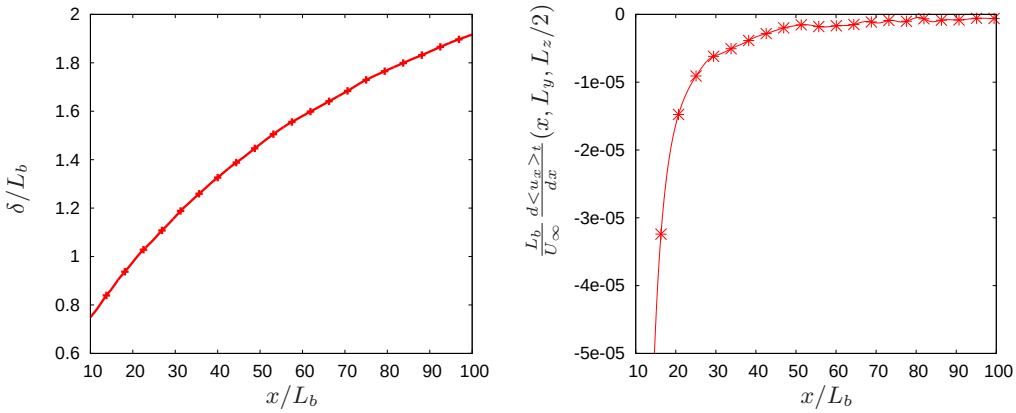

FIGURE 5. Streamwise evolution of the wake width δ/L_b (left) and of $\frac{L_b}{U_\infty}\frac{d<u_x>_t}{dx}(x, L_y, L_z/2)$ (right).

about the code "Incompact3d" can be found in Laizet & Lamballais (2009), Laizet *et al.* (2010) and also in Laizet & Li (2011) concerning its massively parallel version available in code Licence GNU GPL v3 (see the link `http://code.google.com/p/incompact3d/`).

The collection of data for the turbulent statistics is done over a time of $T = 3850L_b/U_\infty$, corresponding to approximately 25 seconds in the experiments and to 423 cycles based on the Strouhal number $St = f_{vs}L_b/U_\infty = 0.11$ associated with the vortex shedding frequency f_{vs} (see Nedić *et al.* (2013*b*)).

To quantify the domain's lateral dimensions in multiples of $\delta(x)$, the streamwise evolution of δ is plotted in figure 5. At $x = 100L_b$ (the most distant streamwise location that we are considering in the present paper), $\delta \approx 1.92L_b$. This means that the domain half-width is $L_y/2 = L_z/2 = 7.5L_b \approx 3.9\delta$ at $x = 100L_b$. According to Redford *et al.* (2012) (p.8), the critical value needed to ensure that the lateral boundary conditions do not affect the wake development is $L_z/2 = L_y/2 \approx 2.95\delta$. The lateral dimensions of our domain therefore appear sufficiently large to avoid any significant contamination from the lateral boundaries even at $x = 100L_b$.

To further interogate possible effects of wake confinement, the streamwise evolution of $\frac{d<u_x>_t}{dx}(x, L_y, L_z/2)$ (i.e. the x-derivative of the local streamwise velocity at the domain edge) is plotted in figure 5 (right). It can be seen that the value of the x-derivative is very small and negative at all streamwise locations considered in our study ($\approx -10^{-5}U_\infty/L_b$). Secondly, close to the plate, the x-derivative is bigger because the velocity deficit is higher in agreement with mass conservation. At $x > 40L_b$, the value of the x-derivative is below $\approx -10^{-5}U_\infty/L_b$ and slowly tending to 0 as expected in the absence of confinement problems.

To assess the statistical convergence of the DNS data, statistics have been computed for three different averaging periods, $T = 850L_b/U_\infty$, $T = 2400L_b/U_\infty$ and $T = 3850L_b/U_\infty$. The streamwise evolutions of the centreline velocity deficit and the wake width are plotted in figure 6 for the three cases. These mean quantities appear converged over the entire streamwise extent considered even for $T = 850L_b/U_\infty$. The same conclusion can be reached for the convergence of the centreline turbulent kinetic energy and dissipation. It must however be pointed out that $T = 850L_b/U_\infty$ and even $T = 2400L_b/U_\infty$ are not sufficient to converge the dissipation profiles at $x = 90L_b$ and $x = 100L_b$ even though $T = 850L_b/U_\infty$ is sufficient at smaller values of x/L_b.

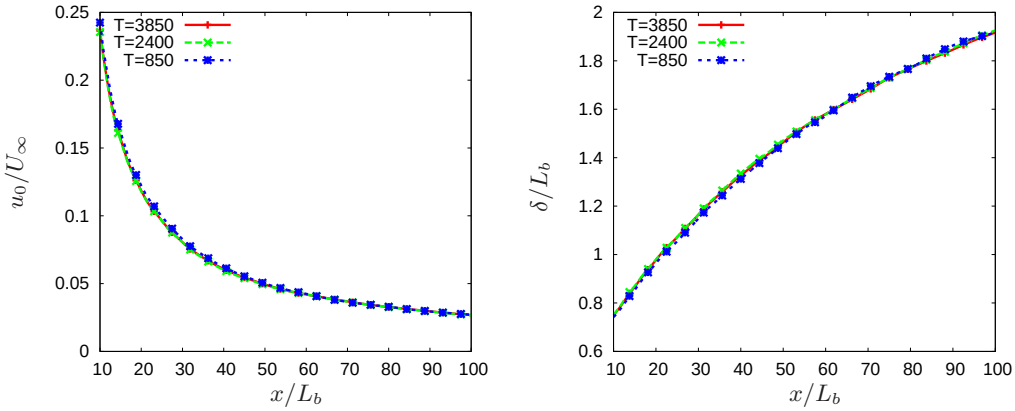

FIGURE 6. Streamwise evolution of the centreline velocity deficit u_0 (left) and wake width δ (right) for three different averaging periods.

4. Experimental setup

The experiments have been run in a low turbulence wind tunnel with a measurement test section of 3×3 ft^2 ($\sim 91 \times 91$ cm^2) and length 4.25 m. The experimental setup is based on the one used in Nedić *et al.* (2013*b*). The plate has a reference length $L_b = 64$ mm with thickness 1.25 mm. The irregular plate is suspended in the center of the wind tunnel normal to the laminar free stream using four 1 mm diameter piano wires. Free-stream velocity was kept fixed at $U_\infty = 10$ m/s. For that value, the velocity fluctuations around the mean are below 0.1 % when the test section is empty.

Hot wire anemometry measurements were taken downstream of the wake generator using a Dantec Dynamics 55P01 hot-wire probe, driven by a Dantec StreamLine CTA system. The Pt-W wires were $5\mu m$ in diameter, 3 mm long with a sensing length of 1.25 mm. The centerline of the wake was found by searching the maximum of the velocity deficit u_0 by successive iterations and with cross-wire checks described two paragraphs below. To obtain mean turbulent wake profiles, the probe was traversed at each one of the streamwise locations $x/L_b = 10, 15, 20, 25, 30, 35, 40, 45, 50$ in 10 mm vertical intervals normal to the streamwise x axis between $y = -250$ mm and $y = 250$ mm. For each probe location, the acquisition time was 60 s with a sampling rate of 20 kHz. Therefore each profile acquisition took about 1 hour of measurements. Two calibrations (one at the beginning and one at the end) were made for each profile, while temperature was monitored to not exceed a variation of 0.2°C. The results reported here correspond to the lower half of the profiles measured, while the whole profile was used to check the positioning of the centre of the wake.

The axisymmetry of the flow was studied by taking radial-polar profiles at $x/L_b = 10$ and 30. Measurements for these profiles were taken at 8 different radial positions (5, 10, 20, 35, 50, 75, 100 and 150cm) and 25 polar angles equispaced between $-\pi$ and π with the same wire. Taking into account the centreline position, this gives 193 points at each streamwise position. Each point measurement has been acquired for 30 sec at 20 kHz and a new calibration has been taken each 30 min with the same procedure as the one described in the previous paragraph for temperature variations.

Finally, a 55P51 x-wire probe (with same wires as that of our single wire probe) was used for centreline measurements. At each centreline position, 30 min of data were acquired at 20 kHz. A new calibration was performed at every centreline position and

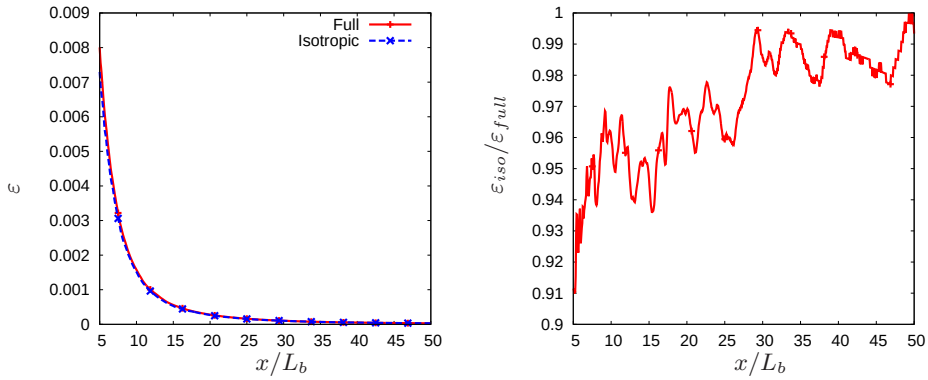

FIGURE 7. Centreline evolution of the full and isotropic dissipation (left) and of the ratio $\varepsilon_{iso}/\varepsilon_{full}$ (right). DNS data.

temperature variations were monitored as explained above. The x-wire measurements were used to calculate the centreline kinetic energy by assuming axisymmetry as $K_0 = 0.5\left(< u_x'^2 > +2 < u_r'^2 >\right)^{1/2}$ where u_x' and u_r' are, respectively, the streamwise and the radial fluctuating velocities.

The turbulent energy dissipation was only estimated on the centreline from single wire measurements acquired over 30 min with 20 kHz sampling rate. It was calculated as $\varepsilon_{iso} = \int 15\nu k_1^2 E_{11} dk_1$ where $E_{11}(k_1)$ is the the $1D$ power spectrum and $k_1 = 2\pi f/U$ where f is a Fourier frequency in Hz. We therefore assume local isotropy at the centreline and we use the Taylor hypothesis (the turbulence intensity based on the local mean flow velocity is always below, and in most cases much smaller than 12%). The validity of the local isotropy assumption was checked with our DNS data and in figure 7 we compare $\varepsilon_{iso} = 15\nu \left\langle (\partial u_x'/\partial x)^2 \right\rangle$ with the actual dissipation rate $\varepsilon_{full} = 2\nu \langle s_{ij} s_{ij} \rangle$ where $s_{ij} = (1/2)\left(\partial u_i'/\partial x_j + \partial u_j'/\partial x_i\right)$. It is clear from figure 7 (right) that $\varepsilon_{iso}/\varepsilon_{full}$ lies between 0.94 and 1 in the range $10 \leqslant x/L_b \leqslant 50$ and that it quickly tends to 1 as x/L_b increases.

The acquisition time of the centreline single wire measurements being 30 min, an order of 100,000 integral time scales at each streamwise position were recorded thereby allowing good large-scale resolution. The Kolmogorov frequency was always smaller than half our sampling frequency (which is 20kHz) except at the position closest to the plate ($x/L_b = 10$) where it was 12kHz. At this position where our Kolmogorov microscale η is at its smallest, $\eta = 140\ \mu m$, but it grows with streamwise distance to reach $\eta \approx 0.4mm$ at $x/L_b = 50$. We checked that the main contribution to the integral $\int 15\nu k_1^2 E_{11} dk_1$ comes in all our cases from wavenumbers $k_1\eta \leqslant 0.5$ and that variations to the dissipation spectrum at wavenumbers higher than $k_1\eta = 0.5$ modeled by various exponential shapes imply variations in our estimates of ε_{iso} of less than 6%.

5. Reynolds-averaged momentum equation balance

The analysis which leads to the streamwise scalings of the velocity deficit and width of turbulent wakes is usually carried out on the boundary layer approximation of the Reynolds-averaged momentum balance (see Townsend 1976; Pope 2000). In this section we use our DNS to check and confirm the leading and neglected terms in this balance equation.

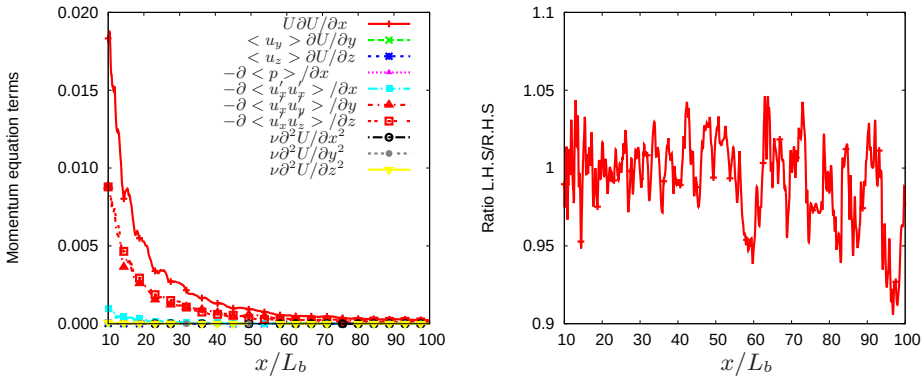

FIGURE 8. Centreline evolution of each term involved in the full Reynolds-averaged momentum equation (5.1) (left) and of the ratio L.H.S/R.H.S (right). DNS data.

In Cartesian coordinates, the full Reynolds-averaged streamwise momentum equation is given by

$$\frac{\partial U}{\partial t} + U\frac{\partial U}{\partial x} + \langle u_y \rangle \frac{\partial U}{\partial y} + \langle u_z \rangle \frac{\partial U}{\partial z} = -\frac{1}{\rho}\frac{\partial \langle p \rangle}{\partial x} - \frac{\partial \langle u_x' u_x' \rangle}{\partial x} - \frac{\partial \langle u_x' u_y' \rangle}{\partial y} - \frac{\partial \langle u_x' u_z' \rangle}{\partial z} + \nu\left(\frac{\partial^2 U}{\partial x^2} + \frac{\partial^2 U}{\partial y^2} + \frac{\partial^2 U}{\partial z^2}\right) \tag{5.1}$$

where u_x', u_y' and u_z' are the fluctuating velocity components in the x, y and z directions respectively.

For sufficiently converged statistics, the first term on the left hand side vanishes, i.e. $\partial U/\partial t \approx 0$. The centreline evolution of all the other terms is plotted in figure 8 (left) and the ratio between the left hand side (L.H.S) and the right hand side (R.H.S) of equation (5.1) is plotted in figure 8 (right). It can be seen in figure 8 (right) that the full momentum balance (5.1) is represented accurately enough by our calculations on the centreline (the error made in the mean momentum equation budget is almost everywhere below 6%, except at the very end of the domain where it is 10%). It can also be seen in figure 8 (left) that the three terms $U\partial U/\partial x$, $-\partial \langle u_x' u_y' \rangle /\partial y$ and $-\partial \langle u_x' u_z' \rangle /\partial z$ are the main contributors to this momentum balance. We have checked that all the others terms are at least two orders of magnitude smaller than these three terms so that we can use the following simplified equation

$$U\frac{\partial U}{\partial x} = -\frac{\partial \langle u_x' u_y' \rangle}{\partial y} - \frac{\partial \langle u_x' u_z' \rangle}{\partial z} \tag{5.2}$$

This is indeed the simplified form of the mean momentum equation which is typically used to study turbulent wakes. The centreline evolutions of the L.H.S and R.H.S of the simplified balance (5.2) are plotted in figure 9 (left) and their ratio is plotted in figure 9 (right). This figures confirms that the simplified Reynolds-averaged momentum equation (5.2) is valid in our turbulent wake where $L.H.S \approx R.H.S$ for all streamwise locations within 8%. The viscous term, in particular, is always at least two orders of magnitude smaller than these three main terms. We stress this point because it means that the low Reynolds number scalings (1.3) and (1.4) (see Johansson *et al.* 2003, for details) cannot be expected in our data.

To derive scalings for the axisymmetric wake, it is also usual to consider the first order

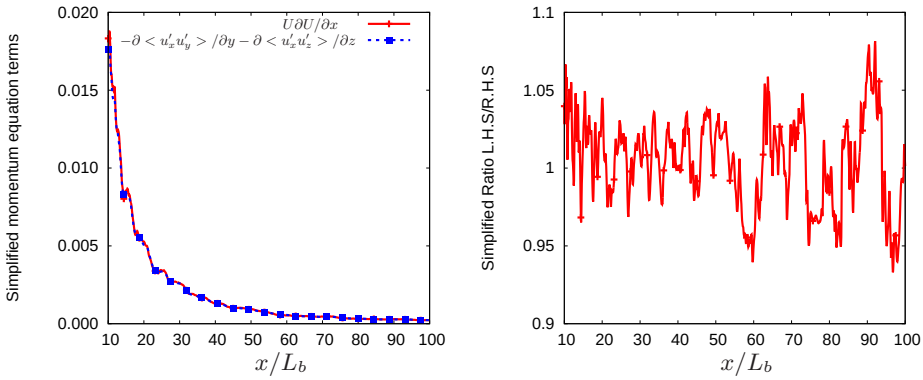

FIGURE 9. Centreline evolution of the L.H.S and R.H.S of the simplified Reynolds-averaged equation for the axisymmetric wake (5.2) (left) and of the ratio L.H.S/R.H.S (right). DNS data.

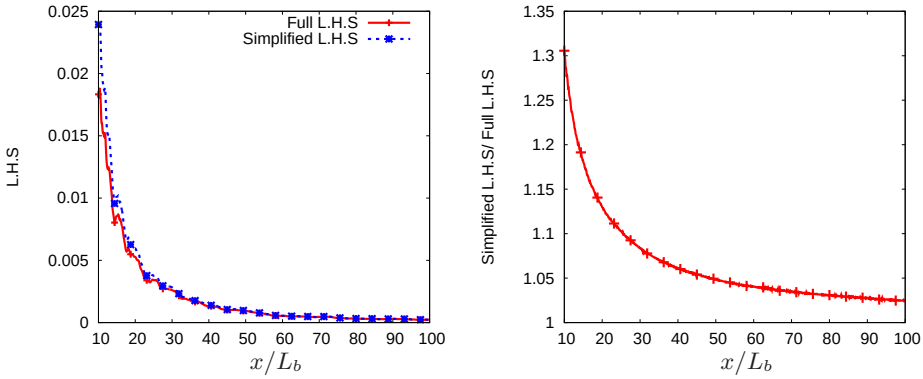

FIGURE 10. Centreline evolution of the full L.H.S $U\partial U/\partial x$ of equation (5.2) and its first order approximation $-U_\infty \partial\left(U_\infty - U\right)/\partial x$ for the velocity deficit of equation (5.3) (left). The centreline evolution of the ratio between the two relations is plotted on the right figure. DNS data.

approximation of equation (5.2) which is

$$U_\infty \frac{\partial}{\partial x}\left(U_\infty - U\right) = \frac{\partial \left\langle u'_x u'_y \right\rangle}{\partial y} + \frac{\partial \left\langle u'_x u'_z \right\rangle}{\partial z} \tag{5.3}$$

in terms of the mean velocity deficit $U_\infty - U$. The centreline evolution of the full L.H.S of equation (5.2) is plotted together with its first order counterpart of equation (5.3) in figure 10. A good agreement is found between both relations with an error that is quickly decreasing and that is always below 10% for $x \geqslant 20L_b$.

6. Axisymmetry of wake statistics

The second step of this analysis is to ascertain the statistical axisymmetry of the wakes generated by our irregular plate. Our DNS provides 3D fields in the entire computational domain, and we use them to check polar variations of the mean velocity U, the Reynolds shear stress $R_{xr} \equiv < u'_x u'_r >$, the turbulent kinetic energy K and the dissipation rate ε. Our HWA measurements provide us with streamwise mean velocities and streamwise Reynolds stresses $R_{xx} \equiv < u'_x u'_x >$ in cross sections of the wake at $x = 10L_b$ and $x = 30L_b$.

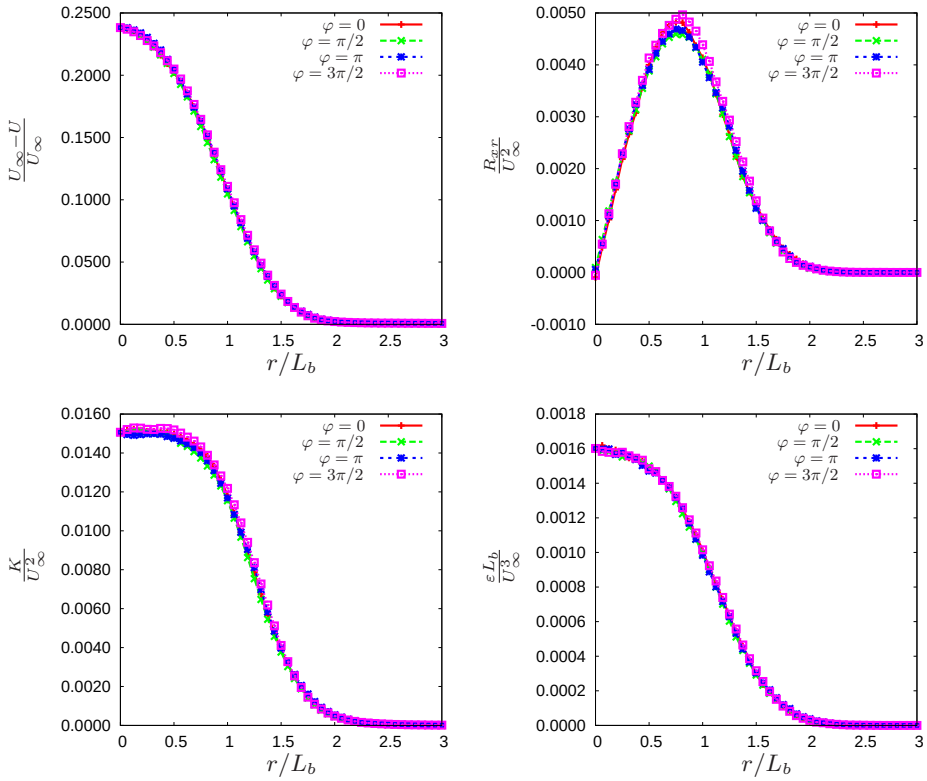

FIGURE 11. Normalised velocity deficit (top left), Reynolds shear stress (top right), turbulent kinetic energy (bottom left) and dissipation rate of turbulent kinetic energy (bottom right) profiles from the DNS case at the downstream location $x/L_b = 10$ for four different polar angles φ.

We use our HWA data in conjunction with our DNS data to both check axisymmetry and agreement between data.

In figure 11 we plot streamwise mean velocity, Reynolds stress, turbulent kinetic energy and dissipation radial profiles at four different polar angles φ, all obtained from our DNS at $x/L_b = 10$. These wake statistics are already quite axisymmetric at this near-field location $x = 10L_b$. As shown in figure 12(left), this observation is confirmed for the mean flow statistics and R_{xx} by our HWA measurements at the same location. This figure also shows satisfactory agreement between the numerical simulation and the experiments.

A more quantitative evaluation of the flow's statistical axisymmetry can be obtained by computing the mean values of the coefficient of variance

$$c_v(x,r) \equiv 100 \frac{\sqrt{(1/N_\varphi)\sum_\varphi \left(S(x,r,\varphi) - \langle S\rangle(x,r)\right)^2}}{\langle S\rangle(x,r)} \tag{6.1}$$

where N_φ is the number of polar angles and S stands for mean flow, kinetic energy or dissipation rate of turbulent kinetic energy. The streamwise variations of the radially averaged coefficient of variance $\overline{c_v}(x) \equiv (1/N_r)\sum_r c_v(x,r)$ are plotted in figure 13 for the DNS and HWA cases (only at $x = 10L_b$ and $x = 30L_b$). It must be mentioned here that the coefficient of variance has not been computed for the Reynolds shear stress component R_{xr} because of the small values it takes close to the centreline leading to

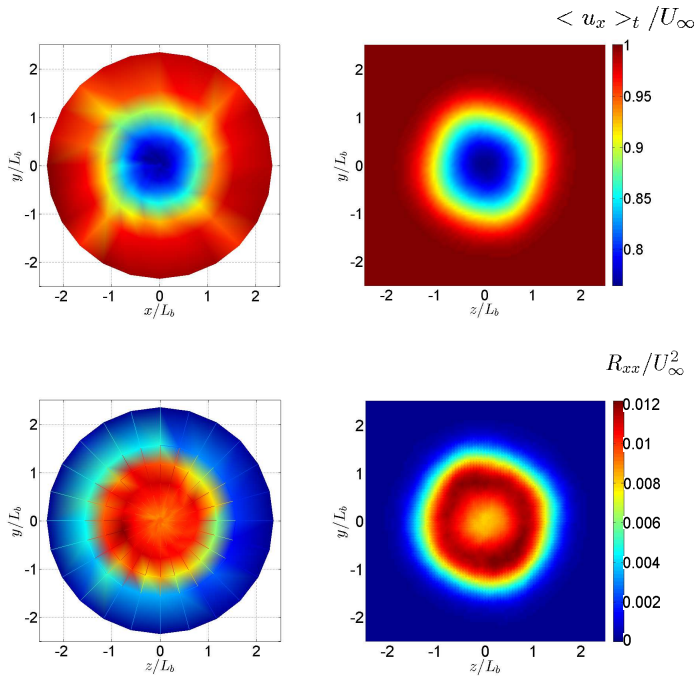

FIGURE 12. Maps of the mean streamwise velocity U/U_∞ for the HWA case (top left) and for the DNS case (top right) with the same colour coding and of the mean streamwise Reynolds stress R_{xx}/U_∞^2 for the HWA (bottom left) and the DNS (bottom right), again with the same colour coding. All these maps are taken at $x = 10L_b$.

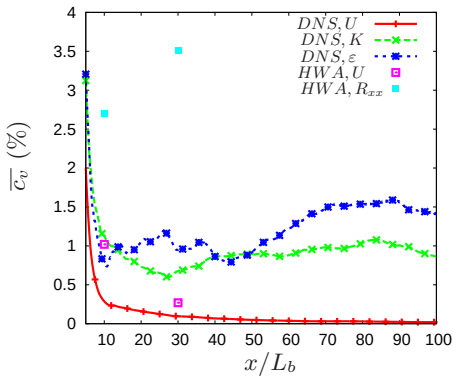

FIGURE 13. Streamwise evolution of the radially averaged coefficient of variance $\overline{c_v}$ for the mean velocity, turbulent kinetic energy and the dissipation profiles of the DNS case and for the mean velocity and streamwise Reynolds stress of the HWA case at $x = 10L_b$ and $x = 30L_b$.

artificially high values of c_v. Because the same problem can appear at large radii where K and ε tend to zero, the radially averaged coefficients of variance are computed for $r \in [0; L_b]$. Figure 13 shows that, at $x = 10L_b$, there is already less than 4% variation in all statistics. Hence, both our DNS calculations and our HWA measurements demonstrate the good axisymmetry of the flow at $x > 10L_b$.

7. Similarity of the axisymmetric turbulent wake

The axisymmetry of the wake having now been demonstrated for both the DNS and the HWA cases, the next step is to investigate the similarity properties of the mean flow statistics. The study of the dissipation law and its consequences on the velocity deficit and wake width scalings follows naturally in the next section. In this section we use our DNS and HWA to analyse the streamwise self-similarity of the mean velocity, Reynolds stress, turbulent kinetic energy and dissipation profiles. Comparisons between our DNS and our HWA data are made for the mean velocity and streamwise Reynolds stress profiles.

The following self-similar forms are considered for the mean velocity, Reynolds stresses, turbulent kinetic energy and dissipation profiles

$$U_\infty - U(x,r) = u_0(x) f(\eta) \tag{7.1}$$
$$R_{xx}(x,r) = G_{01}(x) g_{11}(\eta) \tag{7.2}$$
$$R_{rr}(x,r) = G_{02}(x) g_{22}(\eta) \tag{7.3}$$
$$R_{\varphi\varphi}(x,r) = G_{03}(x) g_{33}(\eta) \tag{7.4}$$
$$R_{xr}(x,r) = R_0(x) g_{12}(\eta) \tag{7.5}$$
$$K(x,r) = K_0(x) h(\eta) \tag{7.6}$$
$$\varepsilon(x,r) = D_0(x) e(\eta) \tag{7.7}$$

where $\eta = r/\delta$ and $f(0) = 1$.

We first investigate whether the profiles (7.1) to (7.7) are self-similar as this is a basic property which must be addressed before embarking on the second question which concerns the actual scalings of the x-dependent prefactors $u_0(x)$, $G_{0i}(x)$ $(i = 1, 2, 3)$, $R_0(x)$, $K_0(x)$, $D_0(x)$. If a profile is self-similar then it must be self-similar with the x-dependent prefactor being the profile's maximum value along r. We can therefore test for self-similarity just by taking $G_{0i}(x) = \max_r(R_{ii})$, $R_0(x) = \max_r(R_{xr})$, $K_0(x) = \max_r(K)$ and $D_0(x) = \max_r(\epsilon)$. The prefactor $u_0(x)$ is a special case as it is the maximum value of $U_\infty - U(x,r)$ anyway, given that $f(\eta) \leqslant f(0) = 1$.

Streamwise mean velocity profiles are plotted in figure 14 for different streamwise distances using the similarity scaling defined in (7.1). These profiles are clearly self-similar for $x \geqslant 10L_b$, with very good agreement between the DNS and the HWA results. The DNS data show that the self-similarity of the mean profiles is maintained in the range $x \in [50L_b; 100L_b]$ where HWA measurements are missing given that the wind tunnel test section is half as long as the DNS domain.

The streamwise, radial and polar Reynolds stress profiles $R_{xx}(x,r)$, $R_{rr}(x,r)$ and $R_{\varphi\varphi}(x,r)$ are plotted in figures 15, 16 and 17. These are normal Reynolds stresses which do not feature in the similarity theory of George (1989) even though the first two do feature in the similarity theory of Townsend (1976). Note the satisfactory agreement between our HWA and our DNS streamwise Reynolds stress profiles (figure 15). Differences between HWA and DNS data can however be noted for $x/L_b < 40$ and $\eta < 1$. These differences could be due to different Reynolds number values in the experiment and the simulation. Our data do not suggest that these Reynolds stresses are self-similar except for the polar one, $R_{\varphi\varphi}(x,r)$, which does appear self-similar for $x/L_b \geqslant 20$. (The streamwise Reynolds stress profiles obtained in the wind tunnel may, arguably, be self-similar for, approximately, $x \geqslant 30L_b$ while the equivalent DNS profiles may perhaps be close to self-similar at $x \geqslant 50L_b$.)

The similarity theories of Townsend (1976) and George (1989) are both based on the average momentum and turbulent kinetic energy equations. George (1989) used the

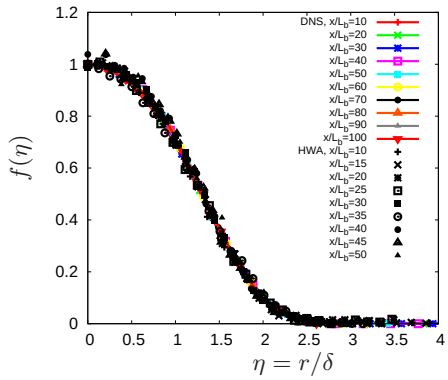

FIGURE 14. Mean flow profiles at different streamwise distances plotted using similarity scaling for both the DNS and the HWA cases.

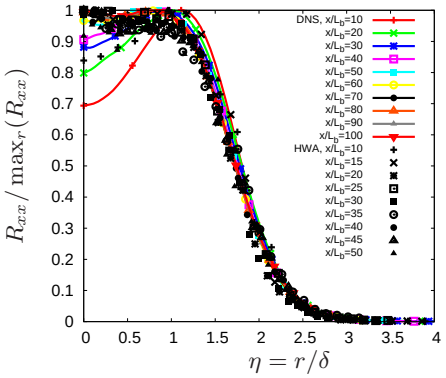

FIGURE 15. Streamwise Reynolds stress profiles at different streamwise distances plotted using similarity scaling with $G_{01} = \max_r(R_{xx})$ for both the DNS and the HWA cases.

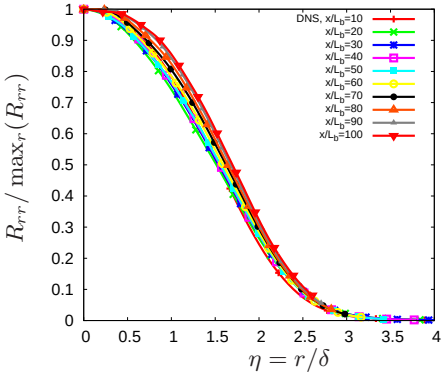

FIGURE 16. Radial Reynolds stress profiles at different streamwise distances plotted using similarity scaling with $G_{02} = \max_r R_{rr}$ for the DNS case.

momentum balance (5.3) which, in cylindrical coordinates (x, r, φ) becomes

$$U_\infty \frac{\partial}{\partial x}\left(U_\infty - U\right) = \frac{1}{r}\frac{\partial r \left\langle u_x' u_r' \right\rangle}{\partial r}. \tag{7.8}$$

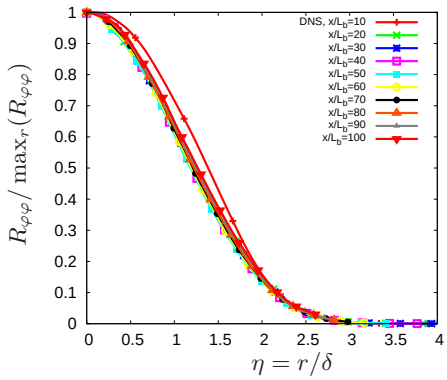

FIGURE 17. Polar Reynolds stress profiles at different streamwise distances plotted using similarity scaling with $G_{03} = \max_r(R_{\varphi\varphi})$ for the DNS case.

and the turbulent kinetic energy evolution equation

$$U_\infty \frac{\partial}{\partial x} K = - \langle u'_x u'_r \rangle \frac{\partial U}{\partial r} + T - \epsilon \tag{7.9}$$

where T and ϵ are, respectively, the transport term and the turbulence dissipation rate, and where the production term is approximated by $- \langle u'_x u'_r \rangle \frac{\partial U}{\partial r}$. His theory therefore relies on this production term approximation and on the self-similarity of the $U_\infty - U$, $\langle u'_x u'_r \rangle$, K, ϵ and transport term profiles. Our DNS provides access to all these quantities except the transport term $T \equiv \frac{\partial}{\partial x_j} \left(< u'_j p'/\rho > + \frac{1}{2} < u'^2_i u'_j > - 2\nu < u'_i s_{ij} > \right)$ which involves spatial derivatives of third order fluctuating velocity statistics and is therefore very expensive to compute because of the large computational time required to obtain converged statistics. (The average momentum and turbulent kinetic energy equations used by Townsend (1976) have a couple more terms which involve the streamwise and radial Reynolds stresses; Townsend (1976) assumed these stresses to be self-similar too.)

The self-similarity of the mean flow profile has already been established. We therefore now consider the self-similarity of the Reynolds shear stress $\langle u'_x u'_r \rangle$, the turbulent kinetic energy K and the dissipation rate ϵ. We plot these profiles in figures 18a, 19a and 20a with R_0, K_0 and D_0 set to be the maximum values along r of $\langle u'_x u'_r \rangle (x, r)$, $K(x, r)$ and $\epsilon(x, r)$, i.e. $R_0(x) = \max_r(R_{xr})$, $K_0(x) = \max_r(K)$ and $D_0(x) = \max_r(\epsilon)$. These figures rather strongly suggest that these three profiles are all self-similar, in the region $x/L_b \geqslant 10$ for $\langle u'_x u'_r \rangle (x, r)$ and $\epsilon(x, r)$ and in the region $x/L_b \geqslant 20$ for $K(x, r)$.

The self-similarity of $U_\infty - U$ and $\langle u'_x u'_r \rangle$ in the region $x/L_b \geqslant 10$ and the validity of the mean momentum equation in the simplified approximate form (7.8) directly imply, as is well known (see George (1989)), that $u_0 \delta^2 = U_\infty \theta^2$ and $R_0 = U_\infty u_0 \frac{d}{dx} \delta$. Figure 18c shows that our DNS supports the prediction $R_0 = U_\infty u_0 \frac{d}{dx} \delta$, at least in the region $x/L_b \geqslant 20$. Incidentally, Figure 18b shows that the assumption $R_0 \sim u_0^2$ made by Tennekes & Lumley (1972) to avoid using the energy equation (7.9) is not supported by our DNS.

The energy equation (7.9) and the self-similarities of K, $U_\infty - U$, $\langle u'_x u'_r \rangle$ and ϵ in the region $x/L_b \geqslant 20$ imply, as is also well known (see George (1989)), that $K_0 \sim u_0^2$ (Townsend (1976) analysis also led to this relation but with more constraining, albeit similar, assumptions). However our DNS does not endorse this scaling, as can be seen in figure 19b. In fact figure 19 shows that K_0 scales in the same way as R_0 in the region $x/L_b \geqslant 20$, i.e.

$$K_0 \sim U_\infty u_0 \frac{d}{dx} \delta. \tag{7.10}$$

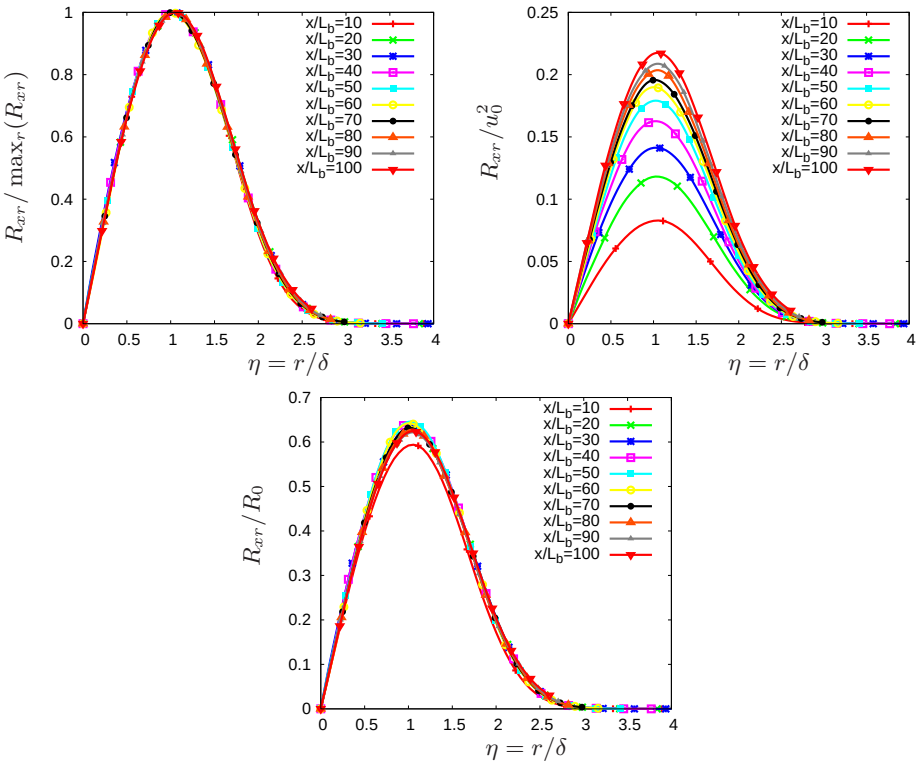

FIGURE 18. Reynolds shear stress profiles at different streamwise distances plotted using similarity scalings with $R_0 = \max_r R_{xr}$ (top left), $R_0 \sim u_0^2$ (top right) and $R_0 \sim u_0 U_\infty \, (d\delta/dx)$ (bottom) for the DNS case.

This is a relation which our higher Reynolds number HWA measurements strongly endorse in the region $10 \leqslant x/L_b \leqslant 50$ where HWA measurements were taken, see figure 21 where centreline HWA and DNS data are plotted together. The scaling (7.10) was also observed in the HWA measurements of Nedic (2013).

The failure of $K_0 \sim u_0^2$ points to a failure of equation (7.9) because the approximation $-\langle u_x' u_r' \rangle \frac{\partial U}{\partial r}$ for the production term is essential in obtaining $K_0 \sim u_0^2$. In fact one cannot expect the production term to equal $-\langle u_x' u_r' \rangle \frac{\partial U}{\partial r}$ on the centreline where $-\langle u_x' u_r' \rangle = 0$. Indeed, as shown in figure 22, our DNS shows that the production term P is dominated by normal stress terms on the centreline and that these normal stress terms are not negligible at $r/L_b = 0.5$ either, in particular $\langle u_x' u_x' \rangle \frac{\partial U}{\partial x}$ which is comparable in magnitude to $-\langle u_x' u_r' \rangle \frac{\partial U}{\partial r}$. We must therefore replace (7.9) by

$$U_\infty \frac{\partial}{\partial x} K = P + T - \epsilon \tag{7.11}$$

and we must not use a self-similarity ansatz for P since, as we have seen, the normal Reynolds stresses R_{xx}, R_{rr} and $R_{\theta\theta}$ are not quite self-similar. Nevertheless the self-similarities of K and ϵ imply that $P + T$ must be self-similar.

Injection of the self-similar forms $K(x, r) = K_0 h(\eta)$ and $\epsilon(x, r) = D_0 e(\eta)$ in (7.11) yields

$$U_\infty \frac{dK_0}{dx} \sim \frac{U_\infty K_0}{\delta} \frac{d\delta}{dx} \sim D_0. \tag{7.12}$$

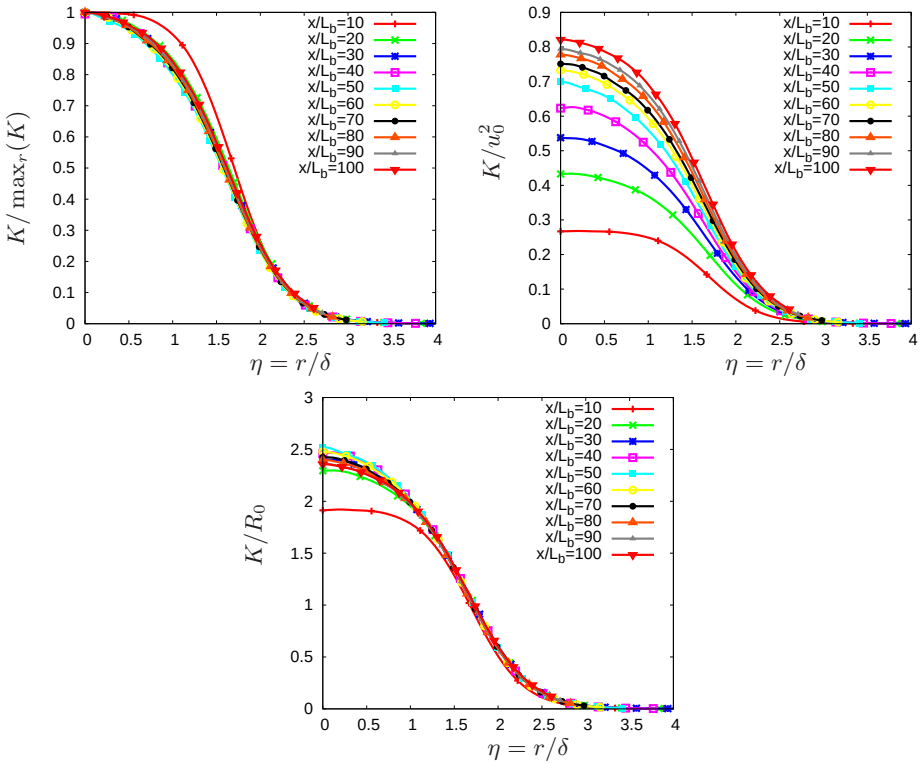

FIGURE 19. Turbulent kinetic energy profiles at different streamwise distances plotted using similarity scaling with $K_0 = \max_r(K)$ (top left), $K_0 \sim u_0^2$ (top right) and $K_0 \sim R_0 \sim u_0 U_\infty$ $(d\delta/dx)$ (bottom) for the DNS case.

Following Nedić *et al.* (2013*b*) we use

$$D_0 \sim (U_\infty L_b/\nu)^m \left(\sqrt{K_0}\delta/\nu\right)^{-m} K_0^{3/2}/\delta \tag{7.13}$$

corresponding to the non-equilibrium dissipation law (1.7)-(2.3)-(2.4) with $n = m$. We limit ourselves to $n = m$ as this is enough for the purposes of this present paper, but it is straightforward to also consider the more general case where the exponents n and m are not necessarily equal.

In the case where $m = 1$, which is also the case reported in the literature at high enough Reynolds numbers (see Vassilicos 2015; Goto & Vassilicos 2015), $D_0 \sim (U_\infty L_b/\nu)\left(\sqrt{K_0}\delta/\nu\right)^{-1} K_0^{3/2}/\delta$ (equation (7.13) with $m = 1$) and $\frac{U_\infty K_0}{\delta}\frac{d\delta}{dx} \sim D_0$ (equation (7.12)) lead immediately to (1.9) which, in turn, leads to (1.8) if use is made of $u_0\delta^2 = U_\infty\theta^2$. These high Reynolds number scalings of $\delta(x)$ and $u_0(x)$ have already been observed in the turbulent wake experiments of Nedić *et al.* (2013*b*).

However, the centreline dissipation rate D_0 does not scale as $D_0^{NEQ1} = (U_\infty L_b/\nu)\left(\sqrt{K_0}\delta/\nu\right)^{-1} K_0^{3/2}/\delta$ in the range $10 \leqslant x/L_b \leqslant 100$ but it does not scale as $D_0^{EQ} = K_0^{3/2}/\delta$ either in that range (see figure 20). These DNS results suggest that when considering the full streamwise range $x \in [10L_b; 100L_b]$, neither the equilibrium dissipation law nor the non-equilibrium dissipation law (at least with $n = m = 1$) are recovered in the axisymmetric turbulent wake generated by our irregular plate. To un-

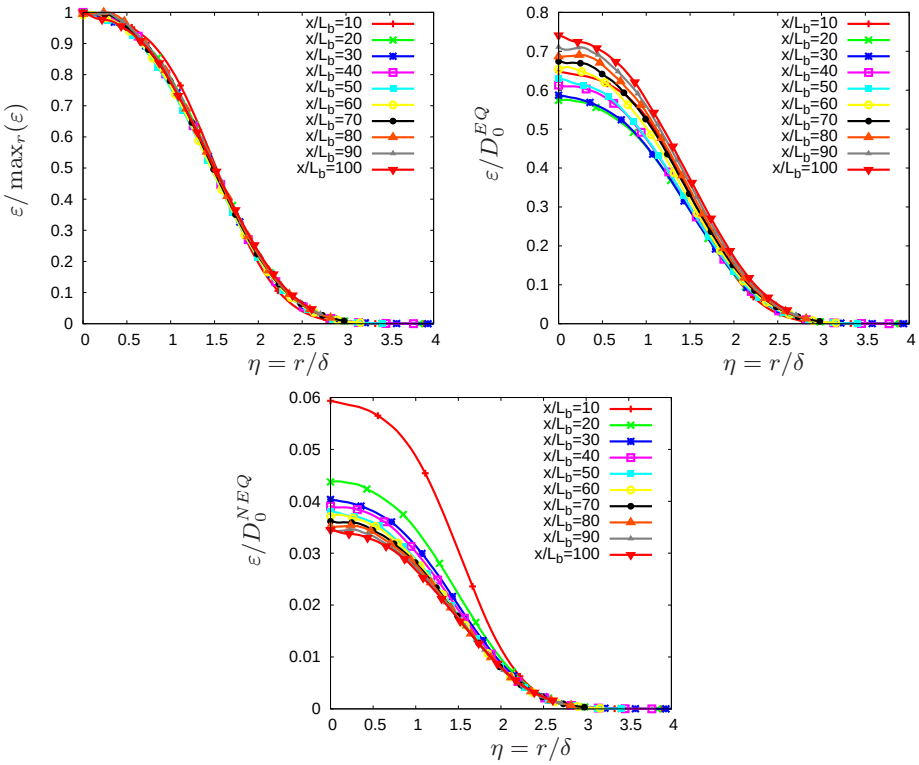

FIGURE 20. Dissipation profiles at different streamwise distances plotted using similarity scaling with $D_0 = \max_r(\varepsilon)$ (top left), $D_0 = D_0^{EQ} = K_0^{3/2}/\delta$ (top right) and $D_0 = D_0^{NEQ1} = (U_\infty l/\nu)\,(u_0\delta/\nu)^{-1}\,K_0^{3/2}/\delta$ (bottom) for the DNS case.

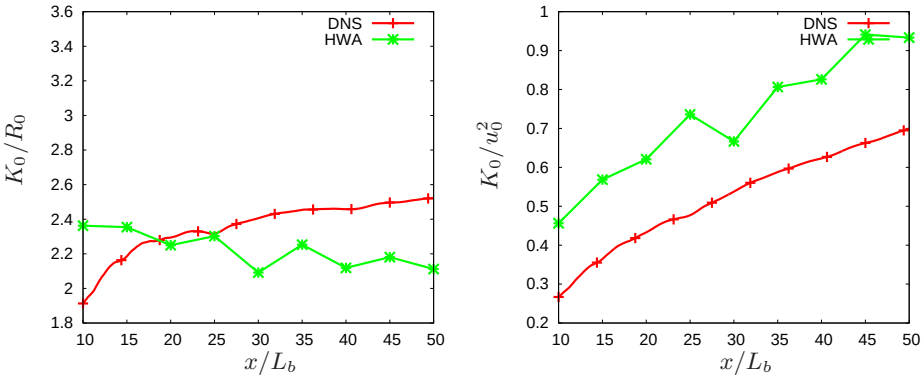

FIGURE 21. Centreline evolution of the ratio K_0/R_0 (left) and K_0/u_0^2 (right) for both the DNS and the HWA cases.

dersand better how the dissipation is evolving in our turbulent axisymmetric wakes, the streamwise evolution of the dissipation is analysed in more detail in the next section.

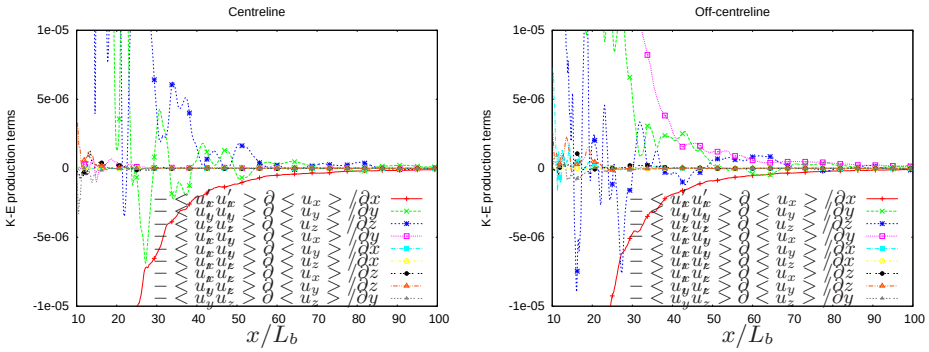

FIGURE 22. Streamwise evolution of each contribution to the turbulent kinetic energy production term for the DNS data on the centerline (left) and at $y/Lb = 0.5$ and $z/L_b = 0$ (right).

8. Streamwise evolution of the centreline dissipation

Defining C_ϵ by

$$\varepsilon = C_\varepsilon K^{3/2}/\delta \tag{8.1}$$

and evaluating it on the centreline $r = 0$ as a function of streamwise distance x generates figure 23 where we plot data obtained by HWA and DNS. The first obvious qualitative observation is that the centreline C_ϵ grows with streamwise distance x even though the local Reynolds number decreases with x (see figure 24), in clear disagreement with the equilibrium law $C_\epsilon = const$. Both the DNS and the HWA data exhibit this behaviour. In fact off-centreline DNS data also plotted in figure 23 show that this behaviour is not specific to the centreline. It is also observed along streamwise $r = L_b/2$ and $r = L_b$ lines. To check if this growth with x can be represented by the non-equilibrium dissipation law (1.7) one needs to check if it is matched by the growth of (Re_G^m/Re_l^n) in the x-direction. We therefore add a plot of $(Re_l^n/Re_G^m) \times C_\varepsilon$ for $n = m = 1$ in figure 23. The HWA data show good agreement with $C_\varepsilon \sim (Re_G/Re_l)$ in the range $15 \leqslant x/L_b \leqslant 50$ and the DNS data are clearly closer to $C_\varepsilon \sim (Re_G/Re_l)$ than to $C_\epsilon = const$ in that range. The better defined $C_\varepsilon \sim (Re_G/Re_l)$ scaling in the higher Reynolds number HWA data than in the lower Reynolds number DNS data agrees with the obervations of Goto & Vassilicos (2015) who found that the local Taylor length-scale-based Reynolds number Re_λ needs to be higher than 100 for $(Re_l/Re_G) \times C_\varepsilon$ to be a sufficiently well-defined constant. Indeed, Re_λ is below 100 in the DNS region $15 \leqslant x/L_b \leqslant 50$, and again in agreement with Goto & Vassilicos (2015), $(Re_l/Re_G) \times C_\varepsilon$ is larger for our DNS than for our HWA data which are characterised by Re_λ values between 200 and 300.

A close look at the DNS data in figure 23 may suggest a slope change at $x/L_b \approx 55$. Downstream of $x \approx 55L_b$ (where Re_λ is below 60), the product $(Re_l/Re_G) \times C_\varepsilon$ appears to be quite clearly slightly decreasing, palpably more than in the region $15 \leqslant x/L_b \leqslant 50$ where it might be closer to a constant. While our DNS and HWA observations support the non-equilibrium dissipation law (1.7) with $n = m \approx 1$ in the region $x \in [15L_b; 50L_b]$, the DNS data suggest a change in the exponents m and n further downstream. We elaborate on this point in the next section.

9. Wake width and velocity deficit scalings

The theoretical arguments developed at the end of section 7 for the prediction of the wake width and the centreline velocity deficit rely on the axisymmetry and self-

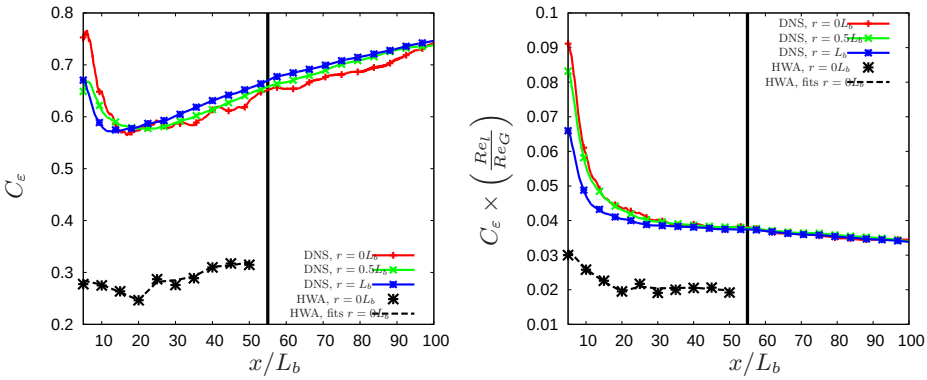

FIGURE 23. Streamwise variation of the dissipation constant C_ε (left) and $C_\varepsilon \times \left(\frac{Re_l}{Re_G}\right)$ (right) for both the DNS and HWA cases. The black vertical line on the right part corresponds to $x = 55L_b$.

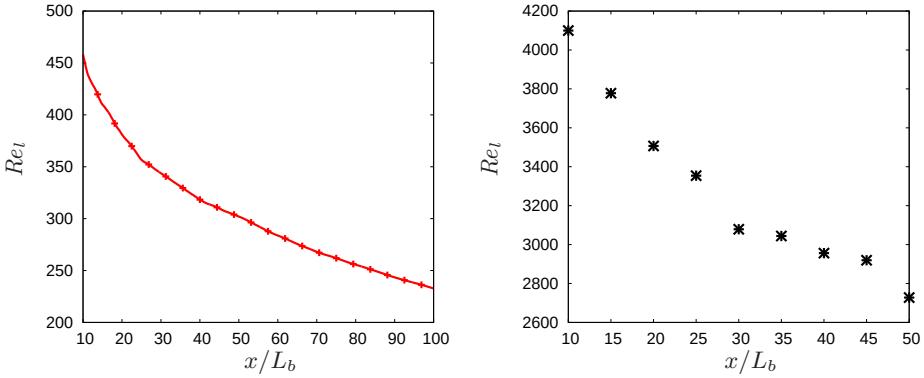

FIGURE 24. Streamwise variation of the local Reynolds number $Re_l = \sqrt{K_0}\delta/\nu$ (left for the DNS and right for the HWA).

similarity of $U_\infty - U$, $\langle u'_x u'_r \rangle$, K and ϵ and the use of the streamwise average momentum and turbulent kinetic energy equations (7.8) and (7.11). All these have been reasonably well verified by our DNS and our HWA measurements in the region between about $10L_b$ and $100L_b$. However, our prediction method also relies on the dissipation scaling and the previous section suggests two different scalings in two different regions, one for $x \in [15L_b; 50L_b]$ and one for $x \in]55L_b; 100L_b]$ (only accessible with our DNS). Since our prediction method has been developed only for the dissipation scaling (7.13) with $m = 1$, i.e. $C_\varepsilon \sim (Re_G/Re_l)$, we now need to extend it to any value of m, i.e. to the non-equilibrium dissipation law (1.7)-(2.3)-(2.4) for any value of $n = m$. Generalisation to $n \neq m$ is straightforward but not necessary in this work.

As already explained in section 7, our revised and modified George theory for $m = 1$ proceeds as follows. Self-similarity of (7.11) yields $D_0 \sim \frac{U_\infty K_0}{\delta}\frac{d\delta}{dx}$ and use of equation (7.13) can only provide a closed set of equations when $m = 1$, in which case it leads to (1.9). In turn, the integral form $u_0\delta^2 = U_\infty\theta^2$ of (7.8) yields (1.8).

When $m \neq 1$ an additional relation is needed and we obtain it on the basis of an assumption of constant anisotropy. According to this assumption, the correlation function between the fluctuating velocity components u'_x and u'_r and the ratios of the r.m.s. values of u'_x, u'_r and u'_φ are constant on $r = \delta(x)$, the surface defining the locations of the

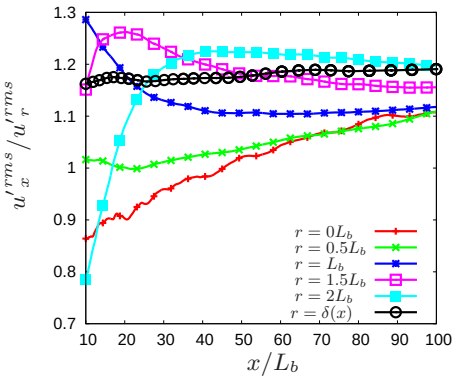

FIGURE 25. Ratios of the r.m.s. of u'_x to the r.m.s. of u'_r as functions of x/L_b along the centreline ($r = 0$) and on various axisymmetric surfaces $r = L_b/2$, L_b, $3L_b/2$, $2L_b$ and $\delta(x)$ for the DNS data. Note how the most constant value of this ratio is found on the surface $r = \delta(x)$.

maximum Reynolds shear stress, over the region considered, i.e. $x \in [15L_b; 100L_b]$ in our case. This assumption and the precise region where it holds will need to be investigated and explained in future studies. Here we note that our DNS data support it (see figure 25) and that it is capable to close our problem for any value of m and return predictions for the wake width and the centreline velocity deficit which agree with numerical calculations and experimental measurements.

The assumption of constant anisotropy implies that the turbulent kinetic energy is proportional to the Reynolds shear stress on the surface $r = \delta(x)$, i.e. $K_0 \sim R_0$. Given that self-similarity of (7.9) implies $R_0 \sim U_\infty u_0 \frac{d\delta}{dx}$, it then follows that $K_0 \sim U_\infty u_0 \frac{d}{dx}\delta$, i.e. equation (7.10) which is supported by both our DNS and our HWA measurements. Combining (7.10) with $D_0 \sim \frac{U_\infty K_0}{\delta}\frac{d\delta}{dx}$ (from the similarity of the turbulent kinetic energy equation) and equation (7.13) leads to

$$\frac{\delta(x)}{\theta} = B\left(\frac{x - x_0}{\theta}\right)^{\beta} \tag{9.1}$$

where $\beta = (1+m)/(3+m)$ and $B \sim (L_b/\theta)^{\frac{2m}{3+m}}$. With $u_0\delta^2 = U_\infty\theta^2$ this relation implies

$$\frac{u_0(x)}{U_\infty} = A\left(\frac{x - x_0}{\theta}\right)^{\alpha} \tag{9.2}$$

where $\alpha = -2\beta = -2(1+m)/(3+m)$ and $A = B^{-2}$. Note that $m = 0$ yields the well-known equilibrium scalings $\delta(x) \sim (x - x_0)^{1/3}$ and $u_0 \sim (x - x_0)^{-2/3}$ and that $m = 1$ leads to the non-equilibrium scalings $\delta(x) \sim (x - x_0)^{1/2}$ and $u_0 \sim (x - x_0)^{-1}$ observed by Nedić *et al.* (2013*b*). The previous predictions (1.5) and (1.6) imply the exact same scalings for $n = m = 0$ and $n = m = 1$.

The different dissipation scalings in the two different regions $x \in [15L_b; 50L_b]$ and $x \in]55L_b; 100L_b]$ suggest different wake width and velocity deficit scalings. In order to investigate these different scalings, the growth of the wake width and the decay of the velocity deficit are now analysed separately in these two different regions of the flow. The following power laws are introduced for the velocity deficit and the wake width

$$\frac{u_0(x)}{U_\infty} = A_1\left(\frac{x - x_{0A1}}{\theta}\right)^{\alpha_1} \tag{9.3}$$

	A_1	α_1	x_{0A1}/θ	B_1	β_1	x_{0B1}/θ
DNS	5.76	-0.94	-2.03	0.42	0.47	-2.03
HWA	7.13	-1.03	-5.10	0.37	0.52	-5.35

TABLE 2. Best fits to u_0/U_∞ and δ/θ obtained using the power laws (9.3) and (9.4) for $x \in [10L_b; 50L_b]$ for both the DNS and HWA cases.

$$\frac{\delta(x)}{\theta} = B_1 \left(\frac{x - x_{0B1}}{\theta} \right)^{\beta_1} \tag{9.4}$$

in the range $x \in [10L_b; 50L_b]$ and,

$$\frac{u_0(x)}{U_\infty} = A_2 \left(\frac{x - x_{0A2}}{\theta} \right)^{\alpha_2} \tag{9.5}$$

$$\frac{\delta(x)}{\theta} = B_2 \left(\frac{x - x_{0B2}}{\theta} \right)^{\beta_2} \tag{9.6}$$

in the range $x \in]55L_b; 100L_b]$. The exponents α_1, β_1 and α_2, β_2 are a priori different, A_1, B_1, A_2, B_2 are dimensionless constants and x_{0A1}, x_{0B1}, x_{0A2} and x_{0B2} are virtual origins. It must be pointed out that our revised George theory also enforces $x_{0A1} = x_{0B1}$ and $x_{0A2} = x_{0B2}$ as in the previous theories of Tennekes & Lumley (1972), Townsend (1976) and George (1989). The DNS and HWA data are fitted with the relations (9.3) and (9.4) in the region $x \in [10L_b; 50L_b]$ and the DNS data are also fitted with the relations (9.5) and (9.6) in the further downstream region $x \in]55L_b; 100L_b]$. Our fitting method is an improvement on the one used by Nedić *et al.* (2013*b*) and returns approximately equal values of the two virtual origins, i.e. $x_{0A} \approx x_{0B}$, as should indeed be the case. The fitting method starts with linear fits of $(u_0/U_\infty)^{1/\alpha}$ and $(\delta/\theta)^{1/\beta}$ versus x for several values of α and β respectively. The values of α and β giving the best linear regression coefficients (closest to 1) are retained and used to calculate A, B and the two virtual origins.

The best fit values for the range $x = 10L_b$ to $x = 50L_b$ are reported in table 2 for both the DNS and HWA cases. The exponents are very close to the non-equilibrium scaling values $\alpha = -1$ and $\beta = 1/2$ predicted by our theory for $m = 1$. The virtual origins turn out to be identical, i.e. $x_{0A1} = x_{0B1}$, in the DNS case and very close to each other in the HWA case. Interestingly, the DNS and the HWA measurements return comparable values of the non-dimensional constants A_1 and B_1 even though the global Reynolds number is 8 times larger in the wind tunnel experiment than in the DNS. Moreover, both the experimental and the numerical data return values of A_1 and B_1 which obey $A_1 \approx B_1^{-2}$ in agreement with the theory.

In figures 26 and 27 we plot $(u_0/U_\infty)^{1/\alpha_1}$ and $(\delta/\theta)^{1/\beta_1}$ versus x/θ using the exponents given in table 2 on the left plots and the equilibrium exponents $\alpha_1 = -2/3$ and $\beta_1 = 1/3$ on the right plots. It is clear from these plots that α_1 and β_1 take values which are very close to the non-equilibrium exponents -1 and $1/2$ respectively. These non-equilibrium exponents are predicted by our revised George theory for $m = 1$. They are therefore consistent with, and presumably a consequence of, the non-equilibrium dissipation law (1.7)-(2.3)-(2.4)-$m = 1$ which seems to fit the dissipation data in figure 23 (right) in the region $x \in [15L_b; 50L_b]$.

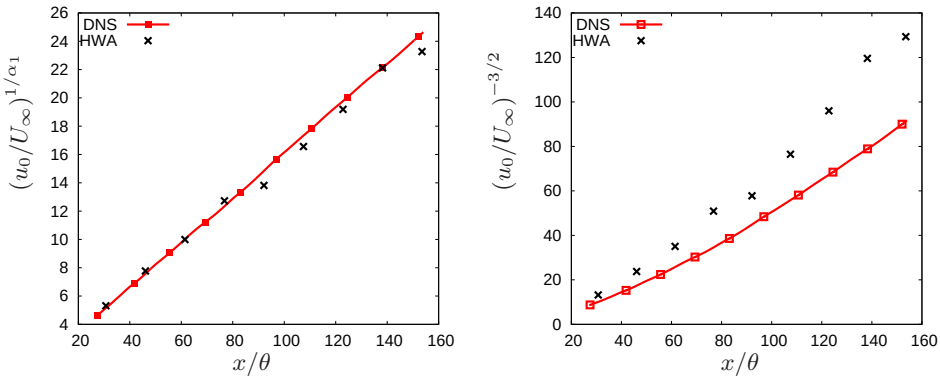

FIGURE 26. $(u_0/U_\infty)^{1/\alpha_1}$ (left) and $(u_0/U_\infty)^{-3/2}$ (right) versus x/θ for $x \in [10L_b; 50L_b]$ for both the DNS and HWA cases.

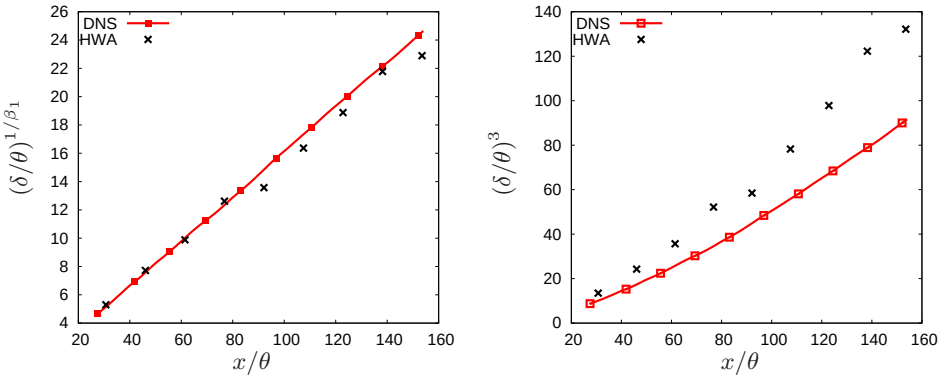

FIGURE 27. $(\delta/\theta)^{1/\beta_1}$ (left) and $(\delta/\theta)^3$ (right) versus x/θ for $x \in [10L_b; 50L_b]$ for both the DNS and HWA cases.

We now focus on the region $x \in]55L_b; 100L_b]$ where the dissipation scaling is neither the classical equilibrium one nor (1.7)-(2.3)-(2.4) with $m = 1$. This far downstream range is accessible with our DNS but not in our wind tunnel experiments and we use 689 DNS data points along the streamwise direction to fit the x-dependence of the velocity deficit and the wake width in the range $x = 57L_b$ to $x = 100L_b$. The position $x = 57L_b$ is the closest to $x = 55L_b$ for which the virtual origins x_{0A2} and x_{0B2} obtained by our fitting procedure are the same. The best fit values are reported in table 3. In agreement with the observation that the new dissipation law (1.7) taken with $m = 1$ does not hold downstream of $x = 55L_b$ (see figure 23 right), the values of the exponents α_2 and β_2 are respectively higher and lower than the values predicted when setting $m = 1$ in (9.2) and (9.1). Note that the values of the constants A_2 and B_2 are in very good agreement with the theory as $B_2^{-2} = 2.87$ in perfect agreement with $A_2 \approx B_2^{-2}$.

The fairly abrupt changes in power laws are manifest in figure 28 where $(u_0/U_\infty)^{1/\alpha_1}$ and $(\delta/\theta)^{1/\beta_1}$ are plotted versus x/θ in the entire range $x \in [10L_b; 100L_b]$. The well-defined linear relationships already seen in figures 26 and 27 are of course found again between $x = 10L_b$ to $x = 55L_b$ but a clearly different evolution is observed for $x > 55L_b$.

The question arises whether the exponents α_2 and β_2 can be explained by our new

A_2	α_2	x_{0A2}/θ	B_2	β_2	x_{0B2}/θ
2.87	-0.81	4.11	0.59	0.41	4.11

TABLE 3. Best fits to u_0/U_∞ and δ/θ obtained using the power laws (9.5) and (9.6) for $x \in [57L_b; 100L_b]$ for the DNS case.

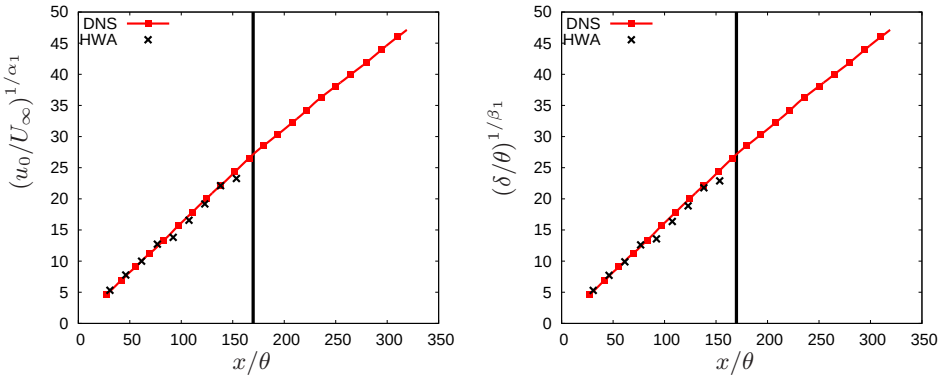

FIGURE 28. $(u_0/U_\infty)^{1/\alpha_1}$ (left) and $(\delta/\theta)^{1/\beta_1}$ (right) versus x/θ for $x \in [10L_b; 100L_b]$ for the DNS case. The black vertical line corresponds to $x = 55L_b$. The experimental data are reminded for illustation purpose for $x \in [10L_b; 50L_b]$.

predictions (9.2) and (9.1) where $\alpha = -2\beta = -2(1+m)/(3+m)$. In other words, could the wake laws observed in the range $x \in]57L_b; 100L_b]$ be accountable to a dissipation law $C_\epsilon \sim (Re_G^m/Re_l^m)$? The value of m which corresponds to our observed $\alpha_2 = -0.81$ is $m = 0.36$, but very small uncertainties in α give rise to high uncertainties in m at such values of m. For example, a 40% variation in m above $m = 0.36$ causes a jump of only 5% in α. The quantity $(Re_l^m/Re_G^m) \times C_\varepsilon$ exhibits a clear plateau in the range $x \in]55L_b; 100L_b]$ for $m = 0.5$ (see figure 29 and compare it with the right plot in figure 23) but not for $m = 0.36$. However, for $m = 0.5$, $-2(1+m)/(3+m) = -0.86$ which is quite close to our observed $\alpha_2 = -0.81$ and we can therefore assume that the dissipation scaling in the range $x \in]55L_b; 100L_b]$ is in fact $C_\epsilon \sim \left(Re_G^{1/2}/Re_l^{1/2}\right)$. This result suggests that the new dissipation law (1.7) still holds in the region $x \in]55L_b; 100L_b]$ but with $m \approx 0.5$ instead of $m \approx 1$. This is confirmed by the good collapse of the dissipation profiles in this region when D_0 is taken to be $D_0^{NEQ2} \sim (U_\infty l/\nu)^{1/2} (u_0\delta/\nu)^{-1/2} K_0^{3/2}/\delta$ (see right plot in figure 30).

In the region $x \in [10L_b; 50L_b]$, where the velocity deficit and wake width scalings might suggest $m = 1$, our DNS does not return a clear collapse of the dissipation profiles when D_0 is taken to be $D_0^{NEQ1} \sim (U_\infty l/\nu)^{1.0} (u_0\delta/\nu)^{-1.0} K_0^{3/2}/\delta$ (i.e. $m = 1$). However, the DNS value of α_1 is not -1 but -0.94 in this region (see table 2) which corresponds to $m = 0.77$ by virtue of $\alpha = -2(1+m)/(3+m)$. If D_0 is taken to be $D_0^{NEQ1} \sim (U_\infty l/\nu)^{0.77} (u_0\delta/\nu)^{-0.77} K_0^{3/2}/\delta$ (i.e. $m = 0.77$) then a good collapse of the dissipation profiles is obtained in the range $x \in [30L_b; 50L_b]$ (see left plot in figure 30).

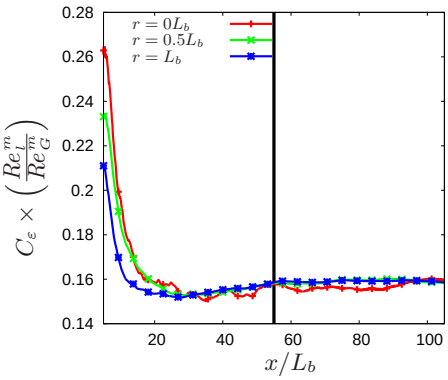

FIGURE 29. Streamwise variation of the product $(Re_l^n/Re_G^m) \times C_\varepsilon$ for $m = 0.5$ using the DNS data. The black vertical line corresponds to $x = 55L_b$.

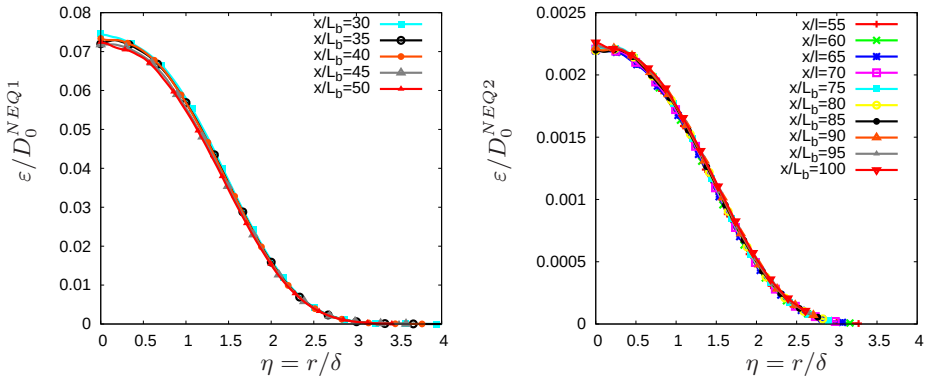

FIGURE 30. Dissipation profiles at different streamwise distances using similarity scaling with $D_0^{NEQ1} \sim (U_\infty l/\nu)^m (u_0\delta/\nu)^{-m} K_0^{3/2}/\delta$ for $m = 0.77$ in the range $x \in [30L_b; 50L_b]$ (left) and with $D_0^{NEQ2} \sim (U_\infty l/\nu)^m (u_0\delta/\nu)^{-m} K_0^{3/2}/\delta$ for $m = 0.5$ in the range $x \in [55L_b; 100L_b]$ (right). DNS data.

10. Summary of results

DNS and HWA measurements of a turbulent wake generated by an irregular plate have been carried out in a flow configuration comparable to the experiments of Nedić *et al.* (2013*b*). The study focused on the assessment of the theoretical assumptions and predictions for the scaling laws of the wake's width and the centreline velocity deficit along the streamwise direction of the flow. A central goal has been to check the consistency of the turbulence dissipation law in the wake with the wake scalings.

Our DNS shows that the isotropic surrogate ϵ_{iso} of the turbulent dissipation is a good approximation of the turbulent dissipation in the region $x \geqslant 10L_b$. It also shows that the approximate streamwise mean momentum equation (5.3) is a good approximation of the mean momentum balance.

The mean velocity, Reynolds shear stress, turbulent kinetic energy and dissipation profiles have been found to become axisymmetric for $x \geqslant 10L_b$. The mean velocity and the turbulence dissipation profiles are self-similar in the region $x \geqslant 10L_b$ whereas the Reynolds shear stresses and turbulent kinetic energy profiles are self-similar in the region $x \geqslant 20L_b$. At least two of the three normal Reynols stress profiles are not self-similar in the streamwise region covered by our study, implying that the turbulence production term is not self-similar either.

Our DNS and HWA data show that the turbulent kinetic energy and the Reynolds shear stress scale together and do not scale as u_0^2. This observation has led us to introduce the assumption of constant anisotropy which implies that $K_0 \sim R_0$. This assumption and the non-equilibrium dissipation law need to be invoked to predict wake width and velocity deficit scalings except when $m = 1$ in which case the non-equilibrium dissipation law is enough. This approach leads to a revised George (1989) theory which yields predictions for the wake width and velocity deficit scalings in agreement with our DNS and HWA data. In particular, in the DNS region $x \in [10L_b; 50L_b]$, $m \approx 0.77$ and $\alpha \approx 0.94$ in agreement with our formula $\alpha = -2(1+m)/(3+m)$ which relates the exponents in equations (9.2) and $C_\epsilon \sim Re_G^m/Re_l^m$. And in the DNS region $x \in]55L_b; 100L_b]$, $m \approx 0.5$ and $\alpha \approx 0.86$ again in agreement with $\alpha = -2(1+m)/(3+m)$. As the local Reynolds number drops with downstream distance, one expects non-equilibrium dissipation scalings to eventually transition to the classical dissipation scaling (see Vassilicos 2015; Goto & Vassilicos 2015) at much further downstream distances.

Acknowledgements

The authors were supported by an ERC Advanced grant (2013-2018) awarded to J.C. Vassilicos. The simulations were performed at the PDC Centre for High Performance Computing at the KTH Royal Institute of Technology (Sweden) with resources provided by the DECI-11 project FRAPLAWI (EC funding RI-312763). The authors also thank PRACE for awarding access to the SuperMUC supercomputer based in Germany at Leibniz-Rechenzentrum (Leibniz Supercomputing Centre) and gratefully acknowledge the valuable help from the technicians of Imperial's Department of Aeronautics for the wind tunnel experiments.

REFERENCES

Bevilaqua, P.M. & Lykoudis, P.S. 1978 Turbulence memory in self-preserving wakes. *Journal of Fluid Mechanics* **89** (03), 589–606.

Brown, G.L. & Roshko, A. 2012 Turbulent shear layers and wakes. *Journal of Turbulence* (13), N51.

George, W.K. 1989 The self-preservation of turbulent flows and its relation to initial conditions and coherent structures. *Advances in Turbulence* pp. 39–73.

Goto, S. & Vassilicos, J.C. 2015 Energy dissipation and flux laws for unsteady turbulence. *Physics Letters A* **379**, 1144–1148.

Gourlay, M.J., Arendt, S.C., Fritts, D.C. & Werne, J. 2001 Numerical modeling of initially turbulent wakes with net momentum. *Phys. Fluids* **13** (12), 3783–3802.

Johansson, P.B.V, George, W.K. & Gourlay, M.J. 2003 Equilibrium similarity, effects of initial conditions and local reynolds number on the axisymmetric wake. *Phys. Fluids* **15** (3), 603–617.

Kravchenko, A.G. & Moin, P. 1997 On the effect of numerical errors in Large Eddy Simulation of turbulent flows. *J. Comp. Phys.* **131**, 310–322.

Laizet, S. & Lamballais, E. 2009 High-order compact schemes for incompressible flows: a simple and efficient method with quasi-spectral accuracy. *J. Comp. Phys.* **228**, 5989–6015.

Laizet, S., Lamballais, E. & Vassilicos, J. C. 2010 A numerical strategy to combine high-order schemes, complex geometry and parallel computing for high resolution DNS of fractal generated turbulence. *Computers and Fluids* **39** (3), 471–484.

Laizet, S. & Li, N. 2011 Incompact3d: a powerful tool to tackle turbulence problems with up to $O(10^5)$ computational cores. *Int. J. Numer. Methods Fluids* **67** (11), 1735–1757.

Laizet, S., Nedić, J. & Vassilicos, J.C. 2015 Influence of the spatial resolution on fine-scale

features in DNS of turbulence generated by a single square grid. *International Journal of Computational Fluid Dynamics, In press* (DOI 10.1080/10618562.2015.1058371).

Lamballais, E., Fortuné, V. & Laizet, S. 2011 Straightforward high-order numerical dissipation via the viscous term for direct and large eddy simulation. *J. Comp. Phys.* **230**, 3270–3275.

Lele, S. K. 1992 Compact finite difference schemes with spectral-like resolution. *J. Comp. Phys.* **103**, 16–42.

Nedic, J. 2013 Fractal-generated wakes. PhD thesis, Imperial College London.

Nedić, J., Ganapathisubramani, B. & Vassilicos, J.C. 2013*a* Drag and near wake characteristics of flat plates normal to the flow with fractal edge geometries. *Fluid Dynamics Research* **45** (6), 061406.

Nedić, J., Vassilicos, J.C. & Ganapathisubramani, B. 2013*b* Axisymmetric turbulent wakes with new nonequilibrium similarity scalings. *Physical review letters* **111** (14), 144503.

Parnaudeau, P., Carlier, J., Heitz, D. & Lamballais, E. 2008 Experimental and numerical studies of the flow over a circular cylinder at Reynolds number 3900. *Phys. Fluids* **20** (8), 085101.

Pope, S.B. 2000 *Turbulent flows*. Cambridge university press.

Redford, J.A., Castro, I.P. & Coleman, G.N. 2012 On the universality of turbulent axisymmetric wakes. *J. Fluid Mech.* **710**, 419–452.

de Stadler, M.B., Rapaka, N.R. & Sarkar, S. 2014 Large eddy simulation of the near to intermediate wake of a heated sphere at Re= 10,000. *International Journal of Heat and Fluid Flow* **49**, 2–10.

Tennekes, H. & Lumley, J. L. 1972 *A first course in turbulence*. MIT press.

Townsend, A.A. 1976 *The structure of turbulent shear flow*. Cambridge university press.

Vassilicos, J.C. 2015 Dissipation in turbulent flows. *Ann. Rev. Fluid Mech.* **47** (1).